Eliminating the TF30 P-111+ Engine Rotor-Instability Problem

J. T. Akin* and V. S. Fehr*
Pratt & Whitney, West Palm Beach, Florida
and
D. L. Evans†
Oklahoma City Air Logistics Center, Oklahoma City, Oklahoma

The TF30 P-111+ engine developed a high-pressure spool rotor dynamic instability when it went into production in mid-1986. Vibration rejection rates were as high as 50% until the instability was eliminated with the incorporation of an oil-film damper at the high-pressure turbine (HPT) bearing. This paper focuses on the analytical treatment of the instability and includes a summary of engine testing that was done to help diagnose the problem. Correlation between test and analysis implicates the aerodynamic cross-coupled forces from the HPT system as the destabilizing mechanism. Results from the stability model are presented that show the damper completely suppressing the instability as later confirmed by ground-level tests. This experience points out the subtle characteristic of rotor instability and the need for improved quantification of the destabilizing mechanisms that produce it. The predecessor engine model had been in service for years without the problem, yet it developed a rotor instability with the incorporation of a new HPT that had no obvious impact on engine rotor dynamics.

Nomenclature

b	= trunnion damping coefficient
c	= lateral damping coefficient
D	= stage blade pitch diameter
E	= elastic modulus
F	= force
h	= stage average blade height
k	= lateral stiffness coefficient
M	= moment
P	= pressure
S	= scale factor
$\bar{s}$	= complex whirl frequency
T	= stage torque
β	= thermodynamic efficiency factor gradient
δ	= logarithmic decrement or rotor deflection
ϵ	= material hysteresis factor
λ	= damping exponent
θ	= rotor slope
τ	= trunnion stiffness coefficient
Ω	= damped whirl frequency

Subscripts

brg	= bearing
C	= cross-coupled, as in cross-coupled stiffness
D	= direct, as in direct stiffness
gnd	= ground
HPT	= high-pressure turbine
RC	= rear case
rel	= relative
rot	= rotor
T	= total, as in total pressure
x	= *x* direction
y	= *y* direction

Presented as Paper 88-3166 at the AIAA/SAE/ASME/ASEE 24th Joint Propulsion Conference, Boston, MA, July 11-13, 1988; received July 25, 1988; revision received April 10, 1989.

*Senior Project Engineer, Government Engine Business.
†Aerospace Engineer, United States Air Force.

Introduction

In the life cycle of a production engine such as the TF30, it is common practice to develop derivative models with durability and performance improvements. In the TF30, these improvements were made as model designations proceeded from P-414 to P-100 to P-111+. In the later model, significant improvements in turbine durability were developed, but when it went into production in the middle of 1986, the new engine were being rejected at rates as high as 50%. The cause of this rejection was excessive nonsynchronous or nonintegral vibration (NIV) suggestive of a rotor instability.

Because the major change between the P-111+ and its predecessor was the high-pressure turbine and its shaft attachment, this area became the focus of the investigation into the cause of the NIV. Many ideas were developed and over 30 engine configurations tested to identify the source of the instability and correct the problem. The most significant of these examined the differences in the turbine cooling scheme between the P-111+ and its stable predecessor. The high-pressure turbine (HPT) cooling air is provided by a mechanical device called the tangential onboard injector, or TOBI, shown in Fig. 1 in its P-111+ bill of material (B/M) configuration. The TOBI delivers turbine cooling air to the disk and blade with minimum flow or pressure loss. Because the pressure in cavity "A" was measured and found to fluctuate at the NIV frequency, it became suspect as a driver of the rotor instability and resultant NIV. It was also noted that changes in the fan inlet pressure, P_{T2}, affected the amplitude of the NIV suggesting that the general source of the problem was aeromechanical coupling.

There was also evidence of wear at the bolted flange joint between the HPT disk and the high-pressure rotor shaft. This wear suggested that internal friction in the flange joint was also a contributor to the rotor instabilility.

The most important configurations tested at ground-level conditions included various TOBI hardware designs and an examination of the effect of P_{T2} on the B/M configuration. Results from these tests were compared with analytical predictions as discussed in the next section.

Analytical Approach and Correlation with Test

The purpose of the analytical activity was to quantify the instability drivers, understand their influence by correlation

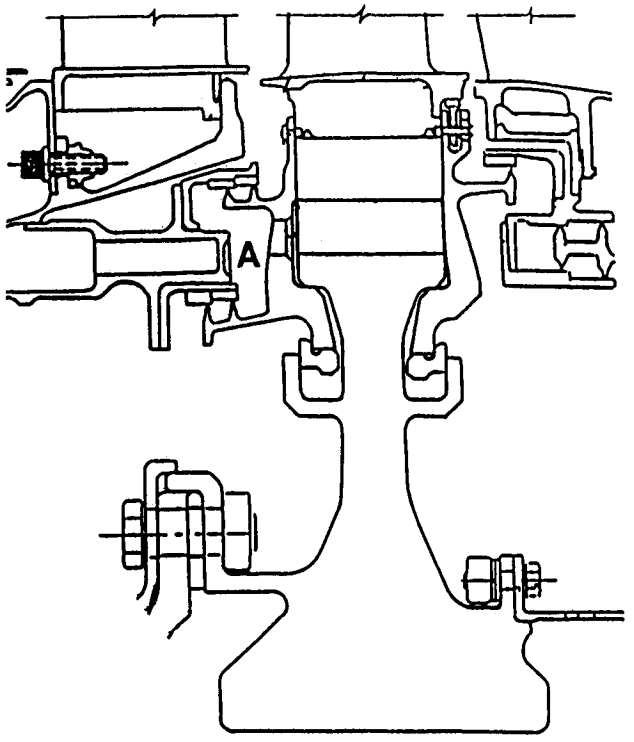

Fig. 1 TF30 P-111+ HPT and tangential onboard injector.

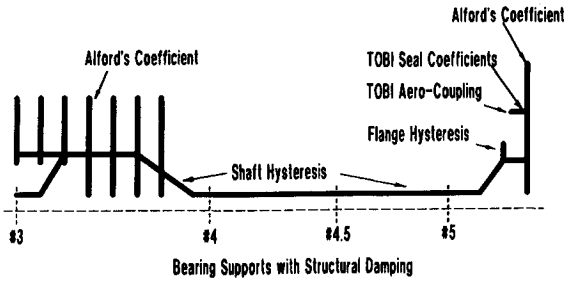

Fig. 2 TF30 P-111+ high rotor instability drivers.

with test results, and recommend a means to eliminate their effect. The first step was to examine the high-pressure rotor of the P-111+ and identify the instability drivers that might be causing the rotor instability. Figure 2 shows a schematic diagram of the high-pressure rotor with its seven-stage compressor and single-stage turbine. Also shown are the instability drivers considered relevant to this problem.

The most famous of these for turbomachinery are Alford's forces[1] which relate the destabilizing force acting on a turbine or compressor stage to the torque extracted from or impressed on the stage. Alford's forces are a subset of the more general aeromechanical coupling or fluid-rotor interaction mechanisms which can occur at other locations in turbomachinery. One of the more visible examples of fluid-rotor interaction was rotor instability in the Space Shuttle main engine turbopumps driven by seal and impeller interaction.[2-4] In the case of the TF30 instability problem, two other aeromechanical drivers besides Alford's forces were considered: the coupling that can occur in the various labyrinth seals around the turbine and the coupling possible with the TOBI hardware.

The seal arrangement around the TOBI establishes a cavity which, in engine ground tests, exhibited a pressure fluctuation at the nonintegral vibration frequency. Furthermore, since the effect of this pressure on the rotor is against the face of dynamically tilting turbine disk, it was judged that it was capable of applying a destabilizing *moment* to the rotor system.

Other instability drivers include shaft hysteresis and the localized hysteresis that may occur due to friction in the bolted flange joint connecting the turbine to the shaft. Bearing supports can also have a hysteresis effect, but because supports do not spin, it manifests itself as stabilizing structural damping.

All of these drivers were included in the analytical model developed to assess the rotor dynamic stability of the high-pressure rotor. On the whole, consideration of the drivers analytically showed that all of the test configurations were unstable and would exhibit the characteristic NIV. Only after an oil-film damper was included at the HPT bearing was the NIV brought under control. In fact, it was predicted to be suppressed by a considerable margin.

Considering the imperative to solve this problem in as timely a fashion as possible, it was decided to use a simple rotor-only model of the high-pressure spool to perform the rotor-stability analysis. The analysis procedure used was that presented by Lund.[5] It calculates the eigenvalues and eigenvectors for the rotor in complex form. The eigenvalue, or complex whirl frequency, is given by

$$\bar{s} = \lambda + j\Omega \tag{1}$$

A common parameter for stability-assessment work is the *logarithmic decrement* or simply *log dec* given by

$$\delta = -2\pi \frac{\lambda}{\Omega} \tag{2}$$

which can be easily computed knowing the components of the complex whirl frequency. With this definition, whirl frequencies and associated mode shapes that have a positive log dec will decay with time and are considered *stable*. Negative log decs then are *unstable*. The log dec parameter is then compared for the engine configurations tested to assess the stability characteristics.

For the TF30 instability assessment, Lund's procedure was extended to include structural damping and trunnion reactions in the supports. The treatment of the supports is particularly important since they are also used to model the aeromechanical coupling effects. Supports introduce a force on the rotor given by the following linear equation:

$$-\begin{Bmatrix} F_x \\ F_y \end{Bmatrix} = \begin{bmatrix} c_D & c_C \\ -c_C & c_D \end{bmatrix} \begin{Bmatrix} \dot{\delta}_x \\ \dot{\delta}_y \end{Bmatrix} + \begin{bmatrix} k_D & k_C \\ -k_C & k_D \end{bmatrix} \begin{Bmatrix} \delta_x \\ \delta_y \end{Bmatrix} \tag{3}$$

Similarly, the moment introduced by the support is given by

$$-\begin{Bmatrix} M_x \\ M_y \end{Bmatrix} = \begin{bmatrix} b_D & b_C \\ -b_C & b_D \end{bmatrix} \begin{Bmatrix} \dot{\theta}_x \\ \dot{\theta}_y \end{Bmatrix} + \begin{bmatrix} \tau_D & \tau_C \\ -\tau_C & \tau_D \end{bmatrix} \begin{Bmatrix} \theta_x \\ \theta_y \end{Bmatrix} \tag{4}$$

In Eqs. (3) and (4), the x and y directions are mutually perpendicular and orthogonal to the rotor centerline.

In this way, the support characteristics are modeled by a set of linearized coefficients. Consider the effect of cross-coupled stiffness shown in Fig. 3. It is the cross-coupled stiffness that causes a force component on the direction of whirl. This force does positive work on the system adding energy and increasing the whirl amplitude with time. This is an instability. Furthermore, moment coupling is directly analogous to force coupling. Thus, this support model can be used with a wide variety of instability drivers.

To obtain the most realistic model possible, the full engine rotor dynamics model of the TF30 was tuned to precisely predict both the forward whirl NIV frequency and its synchronous counterpart observed in engine testing. This was accomplished using rotor dynamics analysis codes based on the technique given by Hibner.[6] Although these frequencies varied somewhat, typical values of 94-Hz nonsynchronous and 4400 rpm synchronous were observed as shown in Fig. 4.

These data were obtained from an accelerometer mounted on the HPT No. 5 bearing support. The left-hand plot in Fig. 4 shows the measured overall response (labeled O/A) and the synchronous response (labeled 1EH) which shows an estimated peak at 4400 rpm. The right-hand plot shows the overall response jumping near 14,500 rpm to greater than 10 mils peak. Filtering this signal showed that it was nonsynchronous at 94 Hz.

Previous analytical studies with this model showed that the frequencies in question were sensitive to the stiffness of the first turbine vane support structure. Adjusting this stiffness value to 77,500 lb/in. resulted in a match of both the synchronous and nonsynchronous test data frequencies. The corresponding nonsynchronous and synchronous modes are shown in Fig. 5. Each line with the different symbols represents a rotor or case structure with the high-pressure rotor and turbine (HPT) annotated. The horizontal axis is the axial centerline of the engine. It can be seen that the high-pressure rotor in both modes has the same general shape, also indicated by the similarity in strain and kinetic energy values.

The high-pressure rotor part of the full engine model was then extracted and used in a rotor-only analysis with supports to ground at the high-pressure spool bearing locations, labeled as #3, #4, #4.5, and #5 in Fig. 2. In order for the rotor-only model to predict the same results as the tuned full engine model, the spring rates to ground must be correctly set. To match the frequency and mode shapes, the rotor must experience the same support force in both models. Thus, the spring rate to ground can be computed using

$$k_{gnd} = \frac{k_{brg}\delta_{rel}}{\delta_{rot}} \tag{5}$$

Two sets of bearing spring rates result from using this procedure, one matching the 94-Hz nonsynchronous mode and the other the 4400-rpm synchronous mode.

Another important consideration is quantification of the instability drivers, a process that must rely on good engineering judgement as well as analysis. In this assessment, only hysteresis and aeromechanical drivers were considered.

As Lund points out for the circular whirl assumption made here, Myklestad's approach[7] using a complex elastic modulus is appropriate for including hysteresis effects, i.e.,

$$\bar{E} = E(1 + j\epsilon) \tag{6}$$

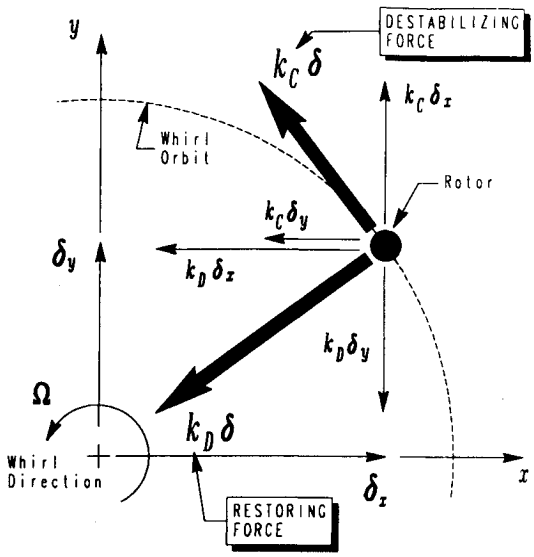

Fig. 3 Cross-coupled stiffness effect.

In the shaft, hysteresis is destabilizing for forward whirl because of the lag between the stress and strain neutral axes caused by the combination of hysteresis and spin.[8] Without spin there is no lag and the hysteresis provides structural damping. The problem is determining a value for ϵ. General experience suggests that values between 0.01 and 0.05 are realistic. The lower values are for solid metal or welded structures, whereas the higher values are for loosely bolted structures. Since gas-turbine engine rotors are tightly assembled to overcome thermal and dynamic effects, a value of 0.02 was used. The supports were given a value of 0.03 since there are more joints with potential hysteresis in the load path to ground.

A range of values from 0.02–0.10 was used in the bolted flange joint along with a two-order-of-magnitude increase in flange flexibility to see if this would influence the rotor stability. The effect on the log dec was always less than 0.02, insignificant compared to the other drivers, so the flange joint was eliminated as a principal influence on the stability of the system. However, it was observed in test that a loose flange could aggravate the NIV problem, but this looseness could be prevented with proper assembly procedures.

Three fluid-rotor effects were considered in this analysis. The first was Alford's forces which were computed using the cross-coupled stiffness equation:

$$k_C = \frac{\beta T}{Dh} \tag{7}$$

Typically, β has values in the range

$$0 \le \beta \le 3 \tag{8}$$

In this analysis, a value of 1.5 was used for the unshrouded turbine configuration and 0.75 for the shrouded turbine (P-414). For the multistage compressor, it was decided to lump the Alford forces at the center stage using the unshrouded

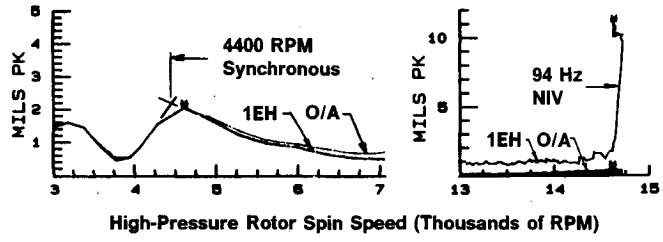

Fig. 4 Typical engine test data.

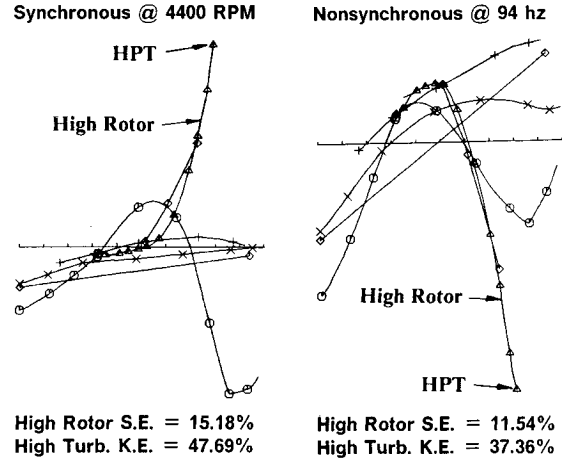

Fig. 5 Matched-frequency mode shapes.

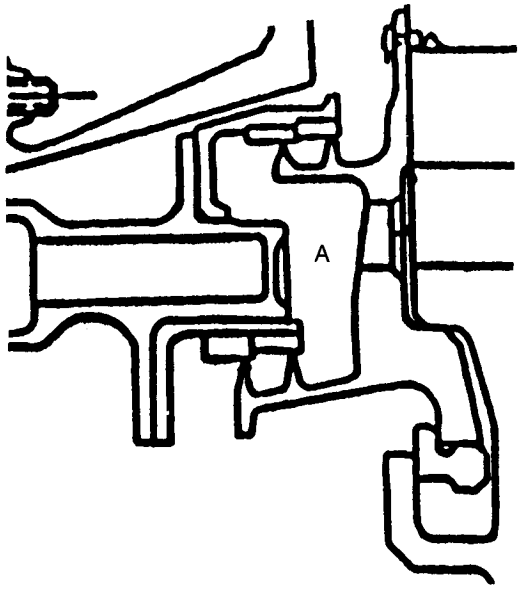

Fig. 6 TF30 P-111+ TOBI system.

value $\beta = 1.5$. This approximation is justified since the compressor has a smaller amplitude compared to the turbine in the modes of interest, minimizing the effect of Alford's forces.

The second interaction considered was that exhibited by the various gas and stratifier labyrinth seals around the turbine stage. Compressor and other seals were ignored for the same reason Alford's forces were lumped in the compressor. Labyrinth seals develop stiffness and damping in both cross-coupled and direct components as given by Eq. (3), unlike Alford's forces which only develop cross-coupled stiffness. Seal stiffness and damping coefficients are a function of clearance, pressure gradient, geometry, and spin speed. They were calculated using a computer program[9] obtained through participation in a research program at the University of Virginia.

The third interaction, suspected as the principal driver of the instability, is the aerodynamic interaction of the TOBI system shown in Fig. 6. In this system, cooling air enters from the left through an orifice on the stationary structure into the cavity marked "A." Cavity "A" is sealed at the i.d. and o.d. by two dual knife-edge labyrinth seals mounted on the turbine side plate. The cooling air then enters the turbine through a hole in the side plate.

No straightforward procedure is available to compute fluid-rotor interaction coefficients for this arrangement, so an estimate had to be made. Pressure measurements in this cavity indicated a fluctuation at the NIV frequency of 94 Hz. Furthermore, the mode shapes show a significant amount of slope due to the high response of the turbine. This suggested that the dynamic pressure could have a sinusoidal distribution around the cavity resulting in a net *moment* acting on the turbine. This, in turn, prompted the extension of Lund's analysis described earlier. The magnitude of this moment was easily calculated using the observed dynamic pressure and the cavity geometry.

Once the moment was calculated, the next step was to determined the stiffness coefficient for this effect for use as τ in Eq. (4). This was accomplished using rear-case (RC) accelerometer data corresponding to the TOBI cavity pressure data in conjunction with the mode shape from the full engine model shown in Fig. 7. Mode shapes, being eigenvalues, are only known to within a multiplicative factor, but knowing the response of the rear case allows calculation of the corresponding turbine slope. First, a scale factor is obtained from the relative amplitudes:

$$S = \frac{\theta_{HPT}}{\delta_{RC}} \tag{9}$$

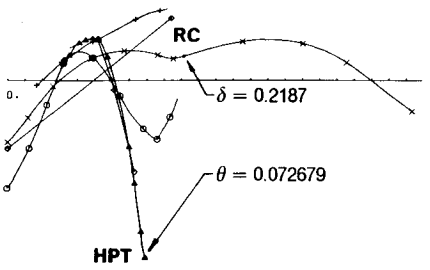

Fig. 7 Moment coupling determination.

followed by

$$\theta_{HPT} = \frac{S}{2}\,\delta_{RC} \tag{10}$$

where the division by 2 is introduced to convert the peak-to-peak response data to single amplitude. Then the moment stiffness coefficient is simply calculated as

$$\tau = \frac{M}{\theta_{HPT}} \tag{11}$$

The remaining question is whether this moment coupling is a direct stiffness or cross-coupled. If the slope (small-deflection theory) is orthogonal to the peak pressure location, the phase is zero and the moment stiffness is all direct. If the slope vector is in line with the peak pressure location, the phase is 90 deg and the stiffness is all cross-coupled. The algebraic sign depends on the quadrant in which the resultant moment falls. For the purpose of analysis, it was assumed that the worst case would be for a fully cross-coupled, destabilizing moment stiffness. This, of course, introduces a phase uncertainty into the estimate.

All of these factors were computed for each of the P-111 + configurations tested with various TOBI configurations and fan inlet pressure values. Results are summarized in Table 1. Also included are results for two predecessor models, the P-414 and P-100, which exhibited only acceptably small NIV amplitudes.

Using the rotor-only model described earlier, each configuration was analyzed to obtain the damped whirl frequency and associated log dec. Results of this analysis are compared with test results in Fig. 8 which shows the analytically predicted logarithmic decrement for each configuration at the top with the corresponding engine test results below. Engine test results are given in NIV amplitude measured in mils peak-to-peak by the rear-case accelerometer.

Reading from left to right, the first two bars are for the P-414 and P-100 models, respectively. They show a predicted log dec smaller than -0.04 (slightly unstable) and a corresponding NIV amplitude of about 1.0 mils. The NIV amplitudes for these models are considered acceptably small and form a reference basis for comparison to the P-111 + results which follow. The third bar shows the results for the B/M P-111 + model and TOBI at full fan inlet pressure. Test data for this configuration shows the highest NIV amplitude at about 12.5 mils and the highest predicted log dec of -0.161, a relatively severe situation. The following two bars show the effect of reducing the fan inlet pressure with the resultant reduction of both predicted log dec and NIV amplitude. Only after a substantial reduction does the NIV amplitude approach an acceptable value. These results served to indicate a dependence on some form of aeromechanical coupling.

With the suspicion of the TOBI mentioned earlier, the TOBI inside diameter seal land was next removed to eliminate the effect of the cavity pressure (bars 6 and 8). This resulted in a definite improvement in the predicted log dec, but still

Table 1 Summary of instability driver parameters[a]

	Alford's lb/in.		Seal stiffness, lb/in.		Seal damping, lb-s/in.		TOBI mom. in.-lb/rab
Hardware	Comp.	Turb.	Direct	Cross	Direct	Cross	Cross
P-414	4653	1318	−200	−52	−1.920	0.920	0.000E+0
P-100	5395	3055	1802	−937	−1.060	4.730	0.000E+0
	5357	3034	5710	−334	−5.570	5.270	1.216E+6
	3623	2052	3802	220	−3.750	3.490	8.147E+5
	2944	1667	3126	189	−3.070	2.840	6.688E+5
	5357	3034	2700	−58	−1.670	2.160	1.089E+5
P-111+	5357	3034	944	800	0.660	0.929	3.053E+5
							1.895E+6[b]
	5357	3034	2700	−58	−1.670	2.160	1.089E+5
	5357	3034	5710	334	−5.570	5.270	1.216E+6
	5357	3034	1108	568	0.570	1.100	0.000E+0
	5357	3034	1519	63	−0.530	1.320	0.000E+0

[a]Structural damping factor = 0.03 and shaft hysteresis factor = 0.02 for all builds.
[b]Phase uncertainty for previous case.

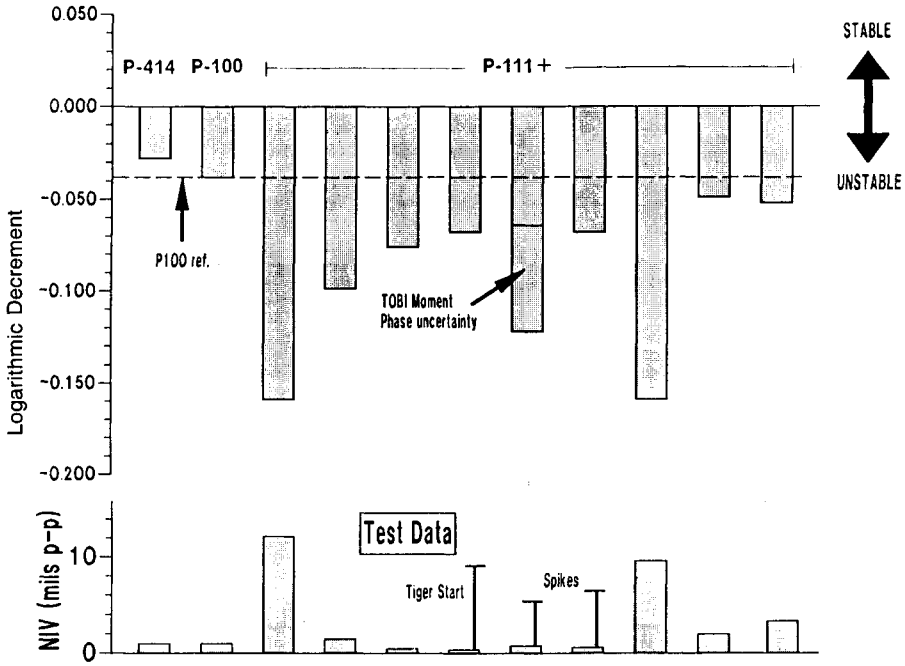

Fig. 8 Comparison of analytical and test results.

showed 9 mil NIV during cold engines starts with an immediate throttle excursion to military power (labeled "Tiger Start" in Fig. 8). Results from another configuration (bar 7) with opposed TOBI knife-edge seals were used to determine the TOBI moment coupling coefficient described above. This bar shows the significant uncertainty in the phase effect which determines how much of the moment coupling is cross-coupled and therefore destabilizing. NIV spikes of significant amplitude were still present in the test data.

The 9th bar indicates a B/M TOBI configuration in which the turbine side plate was modified to include circumferentially raised bumps to minimize contact area with the turbine disk. This was expected to reduce possible destabilizing hysteresis effects due to friction at this surface, but as indicated it had only a minimal effect.

The last two bars show a configuration which eliminates the TOBI inside diameter seal altogether and replaces the outside diameter seal with single and double knife edges, respectively. Predicted log decs for these cases show considerable improvement, but test still showed unacceptable NIV amplitudes of 1.5 to 3.0 mils.

In an effort to identify which one of the instability drivers was the most significant, an analysis was performed which examined the power contributed by each of the drivers. Results of this analysis are shown in Fig. 9. In the P-414 and P-100 models, the TOBI cavity was not sealed and the primary destabilizing power was caused by Alford's forces in the HPT. Similar amounts are present in the P-111+ configurations, but also present are the effect of the TOBI cavity and the seals around it. Shaft or flange joint hysteresis was negligible and is not shown. Only the aeromechanical coupling effects contribute significantly to the destabilizing power, and for each kind, in comparable amounts.

Clearly, none of these configuration changes were able to solve the problem, nor could any of the aeromechanical drivers be identified as the principle contributor to the NIV. Elimination of the TOBI was suggested, but since this TOBI configuration was a contributor to the durability improvement, there was understandable resistance to its removal. It was then decided to examine the possibility of providing an oil-film damper at the No. 5 HPT bearing as a means to control the instability drivers in the B/M TF30 P-111+.

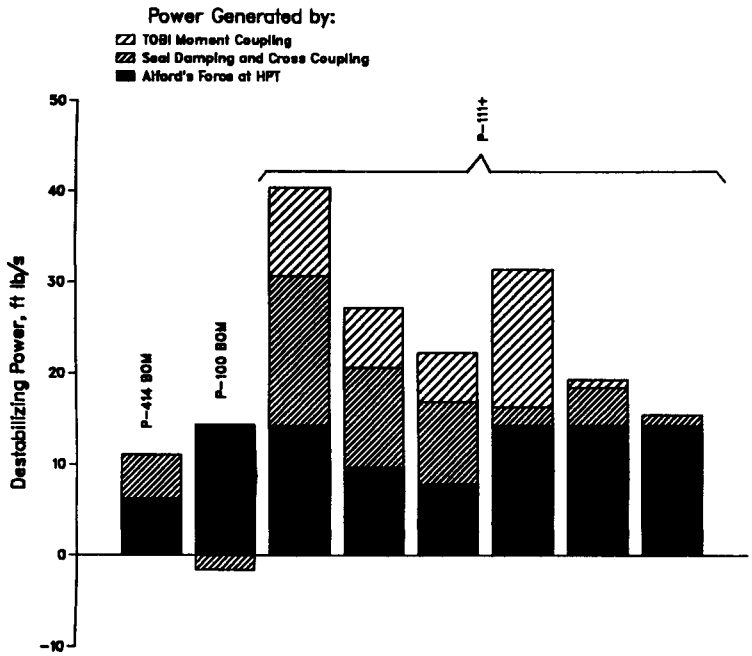

Fig. 9 Destabilizing power comparison.

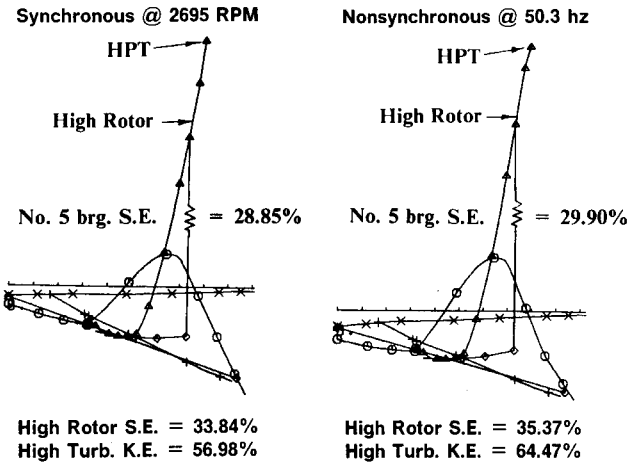

Fig. 10 Damped synchronous and nonsynchronous modes.

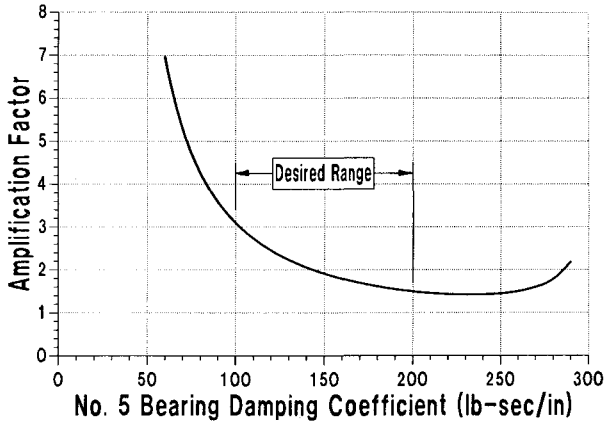

Fig. 12 Effect of No. 5 HPT bearing damping on amplification.

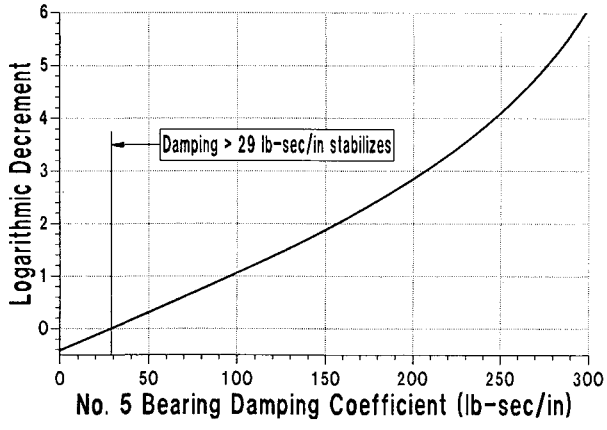

Fig. 11 Effect of No. 5 HPT bearing damping on log dec.

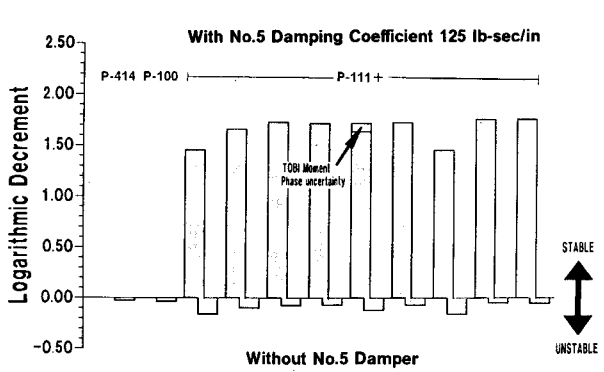

Fig. 13 Analysis prediction with damper.

Damper Analysis and Design

It is well known that the introduction of damping can have a considerable effect on rotor stability. In the TF30 P-111+, the logical place to introduce an oil-film damper was the HPT No. 5 bearing since this was closest to the offending instability drivers. Because of space limitations, such a damper could not have a centering spring, and thus the effective stiffness at the bearing would be that of the oil-film itself. General experience with oil-film dampers of this size suggests an oil-film spring rate of 20,000 lb/in. as a starting point. With this spring rate replacing the 77,500 lb/in. spring rate determined earlier for the undamped support, the full engine model was used to determine the resultant whirl which showed the expected lower frequencies and more energetic modes involving the HPT. These are shown in Fig. 10. Spring rates for the equivalent rotor-only model were then determined as described earlier.

The first step in the design of a damper to control these modes was to determine the necessary damping coefficient. Using the B/M driver values from Table 1, the No. 5 bearing damping coefficient in the rotor-only model was varied to determine the effect on log dec. Results of this analysis, shown in Fig. 11, shows that only 29 lb-s/in. are required to change the log dec from negative to positive. This damping coefficient represents only the threshold value required to achieve rotor stability. Since a comfortable margin was desired to account for the uncertainties in the estimates for the drivers, the amplification for the nonsynchronous mode was examined as a function of the damping coefficient.

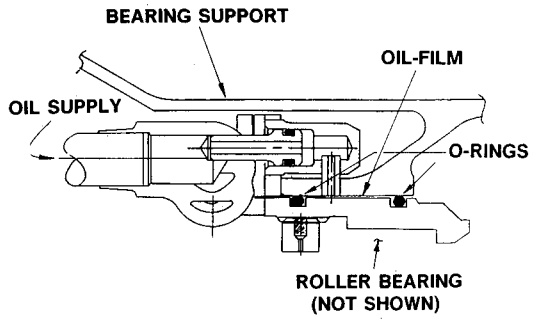

Fig. 14 No. 5 HPT bearing damper configuration.

Plotting the amplification factor, illustrated in Fig. 12, from the same analysis shows that a damping coefficient in the range from 100–200 would keep the amplification factor under the desired value of 3.0. This damping range would also serve to control the synchronous response due to unbalance. Since too much damping could cause the response to rise, the 200 lb-s/in. value was taken as the upper limit.

After choosing 125 lb-s/in. as a reasonable design value, all test configurations were reanalyzed with the results shown in Fig. 13. Also shown for comparison are the predicted results without the damper. Clearly, the damper completely overwhelms the instability drivers and renders the engine stable in all configurations. The phase uncertainty in the TOBI moment is of no consequence, and the damper was recommended as the solution to the NIV problem.

Engine Test Results with Damper

A No. HPT bearing damper without a centering spring and with o-ring end seals was then designed using a proprietary damper design computer program to achieve the desired stiffness (20,000 lb/in.) and damping coefficient (125 lb-s/in.) at the military power condition. This damper configuration is shown in Fig. 14.

A No. 5 bearing damper kit was then developed and installed in several test engines run at ground-level static conditions at the manufacturer's and customer's test facilities. These engines included some with nominal NIV problems and some with NIV amplitudes in excess of 10 mils peak-to-peak. Each engine tested was first run without the damper kit installed to obtain a base NIV condition, then rerun with the kit installed. As predicted by the analysis, the NIV was completely suppressed for engine builds with the damper kit installed, including the engines with originally excessive NIV. These test results are summarized in Fig. 15.

Conclusions

The following conclusions can be drawn from this testing and analysis experience:

1) The cause of nonintegral vibration, when it occurs, is difficult to determine and must be estimated on the basis of comprehensive testing and careful analysis.

2) In the TF30 P-111+ engine, the principal cause of the NIV was the aeromechanical coupling provided by Alford's forces, the tangential onboard injector system in the HPT, and its related gas seals in approximately equal amounts.

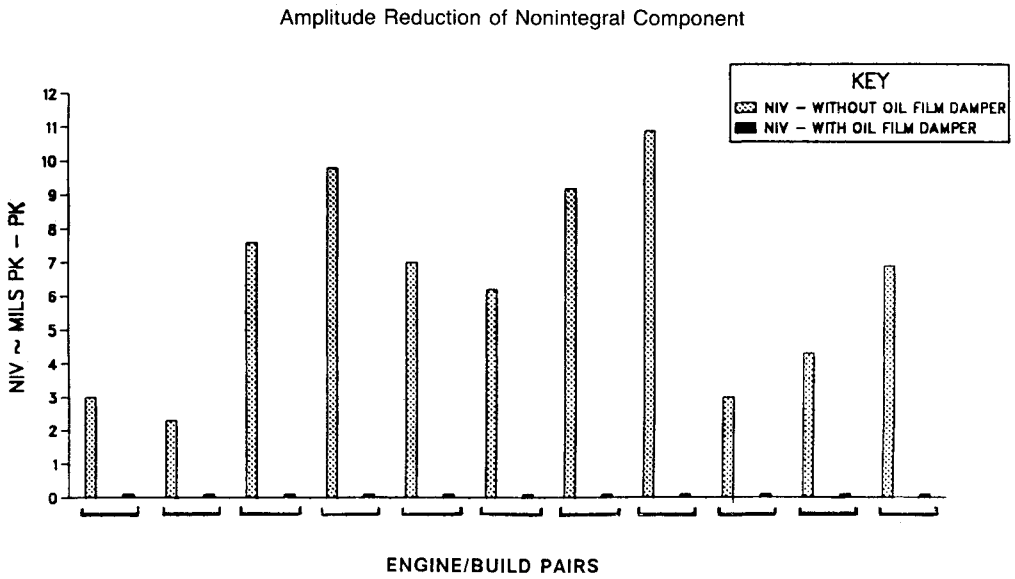

Fig. 15 Engine sea-level test results with and without damper.

3) The variability of the drivers from engine to engine results in varying amounts of instability.

4) The introduction of a carefully designed oil-film damper can completely suppress the instability drivers with sufficient margin to overcome the uncertainty in their analytical estimates and their physical variability.

Acknowledgments

The solution of this extremely complex problem required the concentration, cooperation, and dedication of many people at Pratt & Whitney and the U.S. Air Force. The authors of this paper are only members of that team and are indebted to the rest for providing the data and insights necessary for the successful execution of the analysis described here.

References

[1]Alford, J. S., "Protecting Turbomachinery from Self-Excited Whirl," *ASME Journal of Engineering and Power*, Vol. 87, No. 4, 1965, pp. 333-344.

[2]Childs, D. W., and Moyer, D. S., "Vibration Characteristics of HPOTP (High-Pressure Oxygen Turbopump) of SSME (Space Shuttle Main Engine)," American Society of Mechanical Engineers, New York, Paper 84-GT-31, June 4, 1984.

[3]Childs, D. W., "The Space Shuttle Main Engine High-Pressure Fuel Turbopump Rotordynamics Instability Problem," American Society of Mechanical Engineers, New York, Paper 77-GT-49, March 27, 1977.

[4]Ek, M. C., "Solving Subsynchronous Whirl in the High-Pressure Hydrogen Turbomachinery of the SSME," *Journal of Spacecraft*, Vol. 17, No. 3, May-June 1980, pp. 208-218.

[5]Lund, J. W., "Stability and Damped Critical Speeds of a Flexible Rotor in the Fluid-Film Bearings," *ASME J. Engr. Ind.*, Vol. 96, No. 2, May 1974, pp. 509-517.

[6]Hibner, D. H., "Dynamic Response of Viscous-Damped Multishaft Jet Engines," *Journal of Aircraft*, Vol. 19, No. 3, 1975, pp. 305-312.

[7]Myklestad, N. O., "The Concept of Complex Damping," *ASME Journal of Applied Mechanics*, 1952, pp. 284-286.

[8]Harris, C. M., and Crede, C. E., *Shock and Vibration Handbook*, 2nd ed., McGraw-Hill, New York, 1976, pp. 5-6.

[9]Rosen, M. C., "Calculation of Leakage and Stiffness/Damping Coefficients for Compressible Flow in Straight Through Labyrinth Seals," Univ. of Virginia, Charlottesville, VA, UVA/643092/MAE85/338.